Valence-state Model of Strain-dependent Mn $L_{2,3}$ X-ray Magnetic Circular Dichroism from Ferromagnetic Semiconductors

G. van der Laan,[1] K. W. Edmonds,[2] E. Arenholz,[3] N. R. S. Farley,[2] and B. L. Gallagher[2]

[1]*Diamond Light Source, Chilton, Didcot OX11 0DE, United Kingdom*
[2]*School of Physics and Astronomy, University of Nottingham, Nottingham NG7 2RD, United Kingdom*
[3]*Advanced Light Source, Lawrence Berkeley National Laboratory, Berkeley, California 94720*
(Dated: June 3, 2010)

We present a valence-state model to explain the characteristics of a recently observed pre-edge feature in Mn L_3 x ray magnetic circular dichroism (XMCD) of ferromagnetic (Ga,Mn)As and (Al,Ga,Mn)As thin films. The prepeak XMCD shows a uniaxial anisotropy, contrary to the cubic symmetry of the main structures induced by the crystalline electric field. Reversing the strain in the host lattice reverses the sign of the uniaxial anisotropy. With increasing carrier localization, the prepeak height increases, indicating an increasing $3d$ character of the hybridized holes. Hence, the feature is ascribed to transitions from the Mn $2p$ core level to unoccupied p-d hybridized valence states. The characteristics of the prepeak are readily reproduced by the model calculation taking into account the symmetry of the strain-, spin-orbit- and exchange-split valence states around the zone center.

I. INTRODUCTION

III-V ferromagnetic semiconductors are of widespread interest for applications in spin-based electronics, as well as for fundamental studies of localized-moment ferromagnetism. The ferromagnetic interactions between Mn dopants located at random substitutional sites in the semiconductor lattice are mediated by charge carriers (holes), resulting in a close interplay of magnetism and electrical transport. The nature of the Mn-hole interaction has been the subject of numerous theoretical and experimental investigations.[1–9] The magnetic anisotropy of these materials is of considerable theoretical interest and potential practical importance.[10–12] For the (Ga,Mn)As system, mean-field calculations based on the $\mathbf{k} \cdot \mathbf{p}$ band structure method have proved especially fruitful, allowing quantitative modelling of magnetic, magnetotransport and optical properties with minimal free parameters.[13,14]

X ray magnetic circular dichroism (XMCD) is the difference in the x ray absorption (XA) cross-section of opposite circular polarization with respect to the magnetization direction in the material. This technique offers a number of advantages for the experimental determination of the electronic structure of magnetic compounds: (i) it is element-selective and sensitive to the low magnetic dopant concentrations (1-6%) typically incorporated in a diluted magnetic semiconductor; (ii) it combines chemical and magnetic information, and can distinguish components with differing magnetic behaviors (e.g., ferromagnetic and paramagnetic components); (iii) key parameters including the orbital and spin magnetic moments per atom can be quantitatively obtained by applying the sum rules;[15–17] and it can determine the magnetic anisotropy of the elemental constituents.[18] Studies of ferromagnetic semiconductors have led to the observation of new effects in polarized x ray absorption, including

a crystallographic dependence of x ray magnetic linear dichroism,[19] valence band orbital moments,[20], the separation of components with cubic and uniaxial symmetry in XMCD,[21,22] and Fe induced proximity polarization persisting even above room temperature.[23,24]

We have previously measured Mn $L_{2,3}$ XA and XMCD spectra from (Ga,Mn)As[21,22;24,25] on beamline 4.0.2 of the Advanced Light Source (ALS) at Berkeley, US, beamline ID08 of the European Synchrotron Radiation Facility (ESRF) at Grenoble, France, and beamline I06 of the Diamond Light Source, UK. Figure 1 shows typical XA and XMCD spectra obtained from a (Ga,Mn)As thin film. The main spectral features in the XMCD spectrum are well reproduced by an atomic multiplet calculation (red curve), describing the transition Mn $3d^5 \rightarrow 2p^5 3d^6$ in a tetrahedral crystal field of $10Dq = -0.5$ eV. The spectrum is split into two edges, L_3 around 640 eV and L_2 near 650 eV, due to the large $2p$ spin-orbit interaction.[26]

In the XMCD spectrum a pre-edge feature has been identified near the L_3 edge with different characteristics from the main features in the spectrum (see inset Fig. 1).[21] A similar prepeak behavior in the XMCD is observed for a number of Mn-containing ferromagnetic semiconductors, including (Ga,Mn)As,[21] (Al,Ga,Mn)As,[22] and (Ga,Mn)P[27]. However, this prepeak is not reproduced by the atomic multiplet calculation (c.f., inset of Fig. 1), indicating that it does not belong to the Mn d^5 multiplet structure. The most remarkable experimental findings for the L_3 prepeak XMCD are the following:[21,22]

(i) The prepeak XMCD exhibits a strain-dependent uniaxial angular dependence, with largest intensity when the magnetization is perpendicular-to-plane for tensile strain, and in-plane for compressive strain. In contrast, the main XMCD spectral features show cubic symmetry.

(ii) The prepeak XMCD is positive while the main Mn L_3 XMCD peak is negative, suggesting that the prepeak
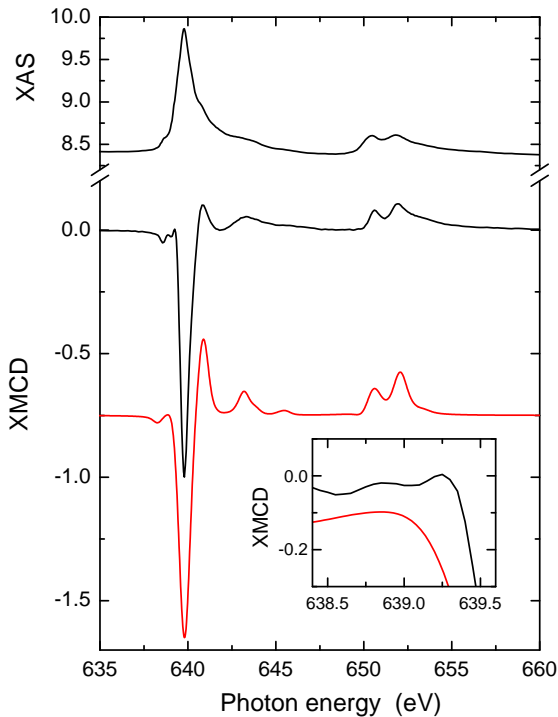
FIG. 1: (Color online) Experimental Mn $L_{2,3}$ XA (upper, black curve) and XMCD (middle, black curve) of a typical (Ga,Mn)As thin film, together with the calculated XMCD multiplet structure for Mn d^5 in tetrahedral crystal field symmetry (lower, red curve). The latter spectrum is offset for clarity. The inset compares the expanded pre-edge XMCD of the experimental (black curve) and calculated (red curve) spectra. Note that the prepeak in the experimental spectrum at 639.3 eV is not present in the calculated XMCD multiplet structure.

originates from states with opposite polarization to the Mn $3d$ local moment.

(iii) The prepeak XMCD shows a dependence on the conductivity of the film. While the prepeak is observed for all (Ga,Mn)As samples studied, it is largest for samples at the insulating side of the metal-insulator transition.

In this paper we will present a straightforward valence-state model, which takes into account the strain-, spin-orbit- and exchange-split hybridized valence states around the Brillouin zone center, and is able to describe all observed effects appropriately.

II. THEORETICAL DESCRIPTION

A. Mn $3d$ state

In soft x ray absorption, the electric-dipole transitions allow excitations of an electron from a $2p$ core level to unoccupied states with s and d character. Since s states are spherically symmetric, only the d states can

cause an angular dependence of the XMCD. A precisely half-filled Mn $3d^5$ state with $S = \frac{5}{2}$ is not expected to show an uniaxial strain-induced splitting due to the absence of an orbital moment and hence lacks the possibility to couple to the lattice. The presence of $3d$ spin-orbit and crystal-field interaction mixes in states with non-zero orbital moment, however for Mn this only results in a very small orbital to spin magnetic moment ratio $m_{\rm orb}/m_{\rm spin} = 1.2 \times 10^{-4}$, as calculated in intermediate coupling using Cowan's code.[28] On the other hand, application of the sum rules[15–17] to the experimental XMCD spectra of (Ga,Mn)As gives a non-zero orbital magnetic moment which is parallel to the spin moment, with $m_{\rm orb}/m_{\rm spin} = 0.03 \pm 0.005$.[21,25,29] This indicates that Mn is not in a pure high-spin $3d^5$ configuration, but has a d count that is slightly higher than five (~ 5.1-5.3) due to hybridization with neighboring As atoms.[12,21,25,29–31]

In the tetrahedral symmetry, the Mn e and t_2 orbitals are separated in energy by the tetrahedral crystal-field interaction of $10Dq \approx -0.5$ eV, where the e state has the lowest energy. The t_2 states hybridize with the As s, p orbitals and can also mix with the Mn $4p$, while the e orbitals are essentially non-bonding. Strain lowers the cubic symmetry, splitting the $d(xy)$ orbitals from the $d(xz, yz)$ orbitals in the t_2 state. However, the strain induced splitting in itself can not give rise to the distinct uniaxial anisotropy of the prepeak if it belongs to the multiplet structure, where all peaks are calculated in same point-group symmetry.[26] In the Mn L_3 XMCD observed for (Ga,Mn)As different features with cubic and uniaxial symmetry can be clearly distinguished by a different angular dependence of the XMCD signal (see App. A).[21] These different features must therefore correspond to Mn $3d$ states with fundamentally different characters.

B. p-d hybridization

In zincblende semiconductors, the top of the valence band is mainly composed of cation $4p$ orbitals. Direct exchange between the holes near the top of the band and the localized Mn d electrons is weak, which allows p-d hybridization to dominate, resulting in an antiferromagnetic coupling.[12] Support for the antiferromagnetic alignment of the As $4p$ spin with respect to the Mn $3d$ is obtained from the As K edge XMCD, which has opposite sign to the Mn $L_{2,3}$ XMCD. Using the sum rule analysis, Freeman $et~al.$[20] found an orbital moment of -1.3×10^{-3} $\mu_{\rm B}$ per As atom for GaAs(001) doped with 8% Mn. Due to the strong spin-orbit interaction, the spin and orbital moment s of the As $4p$ state are parallel.

Figure 2 shows the schematics of a one-electron picture for a Mn d^5 band with hole. The Mn d states are split by the strong exchange interaction and the tetrahedral crystal-field interaction. The filled spin-down Mn d states are deep in the valence band and the empty spin-up d
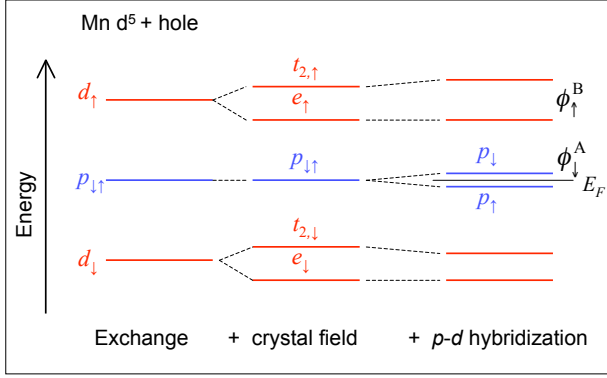
FIG. 2: (Color online) One-electron cartoon: The Mn d states are split by exchange interaction ($\sim$3 eV) and tetrahedral crystal-field interaction ($\sim$0.5 eV) and consequently the Mn acceptor level $|p_\uparrow\rangle$ at the Fermi level, E_F, is split due to the p-d hybridization. The unoccupied states $\phi_\downarrow^A$ and $\phi_\uparrow^B$ correspond to mixed states with predominantly $p_\downarrow$ and $d_\uparrow$ character, respectively. Not shown in the picture is the splitting of the p level by the spin-orbit interaction and strain anisotropy.

states are above the Fermi level, E_F, and high in the conduction band. Hybridization (level repulsion between states of the same spin) between the p and d states pushes up the energy of the spin-down valence p state relative to the energy of spin-up valence p states. Direct crystal-field interaction on the p level is weak, but due to the directional bonding the interaction of the p state with the $d(t_2)$ state is stronger than with the $d(e)$ state. The p-d hybridization splits the Mn acceptor level $|p_{\downarrow\uparrow}\rangle$ at E_F into spin up and down states.

The unoccupied valence states, as shown in Fig. 2, are $\phi_\downarrow^A$ and $\phi_\uparrow^B$. They are a mixture of delocalized As p states and the more localized Mn d states,

$$|\phi_\downarrow^A\rangle = c_{d\downarrow}|d_\downarrow\rangle + C_{p\downarrow}|p_\downarrow\rangle, \tag{1a}$$

$$|\phi_\uparrow^B\rangle = C_{d\uparrow}|d_\uparrow\rangle + c_{p\uparrow}|p_\uparrow\rangle, \tag{1b}$$

where C_n and c_n indicate the wave function coefficients that have a large and small modulus square, respectively, i.e.,

$$|C_{p\downarrow}|^2 \gg |c_{d\downarrow}|^2, \tag{2a}$$

$$|C_{d\uparrow}|^2 \gg |c_{p\uparrow}|^2, \tag{2b}$$

which give the corresponding probability densities. Thus $\phi_\downarrow^A$ and $\phi_\uparrow^B$ and have mainly p and d character, respectively.

The Mn $L_{2,3}$ absorption is due to transitions from the $2p$ core state to unoccupied d states but not to As p states, because the radial overlap of the latter with the Mn $2p$ is too small. In a one-electron model, the XA intensity of the $\phi_\downarrow^A$ and $\phi_\uparrow^B$ states is proportional to $|c_{d\downarrow}|^2$ and $|C_{d\uparrow}|^2$, respectively. Hence, the XA cross-section for the $\phi_\downarrow^A$ state is much smaller than for the $\phi_\uparrow^B$ state. Furthermore, $\phi_\downarrow^A$ is the lowest unoccupied state, which in

a one-electron model for the XA spectrum produces the peak with the lowest photon energy. This indicates—together with other arguments that follow below—that the prepeak feature and the main structure in the XMCD spectrum correspond to $\phi_\downarrow^A$ and $\phi_\uparrow^B$, respectively.

The state $\phi_\uparrow^B$ has a large probability $|C_{d\uparrow}|^2$ [Eq. (1b)], which means that it is mainly localized on the Mn atom, where it is split into e and t_2 states by the local crystal-field interaction. In a many-electron model, Coulomb interactions give a further splitting of the d levels. The localized character requires the use of atomic multiplet theory,[26,32] and as shown in Fig. 1 the calculated XMCD spectrum gives good agreement with the experiment. The main structure will not be further discussed here, as it has already been presented earlier.[21,25]

The state $\phi_\downarrow^A$ has a small coefficient $|c_{d\downarrow}|^2$ [Eq. (1a)], which means that the probability density on the Mn atom is small and therefore this state must be more delocalized. Hence, the symmetry of the $|\phi\downarrow\rangle$ state is hardly affected by the local crystal-field interaction and more influenced by the uniaxial anisotropy of the strain, as is discussed in Sec. II C.

Because the Coulomb interaction for the delocalized valence state is weak—or absent as in the one-electron model—the result is a single feature at the L_3 and L_2 edges, separated by the $2p$ spin-orbit splitting. In the isotropic XA spectrum the small prepeak is dwarfed by the intense main multiplet structure, but in the L_3 XMCD a prepeak at low photon energy can be unambiguously identified due to its different angular dependence.[21,22]

Further support for a hybridized valence state near E_F as given by Eq. (1a) comes from the dependence of the prepeak height on the free-carrier density. It was shown that the prepeak height decreases monotonically with increasing free hole density, obtained from Hall effect measurements.[21] The dependence of the XMCD signal on the conductivity properties is a clear indication that the prepeak involves states lying in the vicinity of E_F. With decreasing free hole density, the conductivity moves towards the insulator side of the metal-insulator transition, and the holes become localized around their parent Mn ions, resulting in an increase in the probability $|c_{d\downarrow}|^2$ at the cost of $|C_{p\downarrow}|^2$, so that the L_3 prepeak XMCD signal will increase.

Also the Mn K edge XMCD shows at low doping a sharp pre-edge due to unoccupied Mn p and d hybridized density of states, and a smaller peak at $\sim$1.4 eV higher energy.[9,20,33] The Mn K pre-edge XMCD strongly increases with lower doping across the metal-insulator transition due to the increase in local d density of states.[33] Simultaneously, the As K edge XMCD decreases.

It is perhaps useful to emphasize the difference between element-specific XMCD and macroscopic magnetic measurements. The anisotropy of the XMCD prepeak is determined by the p-d hybridized valence band states at the zone center, because of the localized character of the core excitation. This is distinct from the strain-dependent

magnetocrystalline anisotropy, which is caused by the anisotropy of the unoccupied valence band states over the whole of the Brillouin zone. The magnetocrystalline anisotropy may be treated by $\mathbf{k} \cdot \mathbf{p}$ theory,[13,34] allowing to calculate perturbatively the band structure in the neighborhood of the zone center, using the energy eigenvalues and basic symmetries of the zone center states. For all but the lowest hole densities, the holes will reside in more than one of the hybridized valence sub-bands, and in states away from $k = 0$. The easy axis of magnetization is thus determined both by the strain and the hole density (i.e., band filling).[13,35] Thus because of the localized character of the $2p$ core excitation, XMCD is a 'local probe' which samples only states with wave vectors near $k = 0$. In certain cases this can lead to large differences between x-ray spectroscopical and macroscopic magneto-optical measurements.[36]

In order to elucidate the XMCD prepeak anisotropy we have to include also the other interactions acting on the p state, in particular the spin-orbit interaction and strain anisotropy, which will be the subject of Sec. II C.

C. Valence state model

We will use here the following approach. First, the sublevel energies of the pure As $4p$ valence state are calculated in the presence of strain and p-d exchange interaction. Due to the large spin-orbit interaction of the As $4p$, the $j = \frac{3}{2}$ level can be considered in a four-band model. Calculations for different magnetization directions give a reversal of the exchange split energy levels between compressive and tensile strain. The XMCD probes the unoccupied states, so that only levels above E_F have to be taken into account. The magnetic moment dependence of the unoccupied levels is obtained by taking the derivative of the energy with respect to the magnetization. The large difference between in-plane and perpendicular magnetization evidences a strong magnetic anisotropy. By comparing the combined influence of strain anisotropy and exchange interaction on the As p and Mn d valence states, we demonstrate that the strain reverses the anisotropy of the prepeak XMCD.

1. As 4p state energies

The magnetic anisotropy of the valence As $4p$ states is calculated using a model Hamiltonian,

$$\mathcal{H} = \mathcal{H}_\text{s-o} + \mathcal{H}_\text{exch} + \mathcal{H}_\text{strain} + \mathcal{H}_\text{hybr}, \tag{3}$$

which contains the spin-orbit interaction, exchange interaction, strain anisotropy, and p-d hybridization. The first term in $\mathcal{H}$ represents the spin-orbit interaction,

$$\mathcal{H}_\text{s-o} = \zeta \mathbf{L} \cdot \mathbf{S} = \tfrac{1}{2}\zeta(\mathbf{J}^2 - \mathbf{L}^2 - \mathbf{S}^2), \tag{4}$$

where ζ is the radial spin-orbit parameter and $\mathbf{L}$ and $\mathbf{S}$ are the orbital and spin angular momentum operators,

respectively. For the pure $j = \frac{3}{2}$ and $j = \frac{1}{2}$ levels of the p state the spin-orbit interaction gives energies of $\frac{1}{2}\zeta$ and $-\zeta$, respectively. The large spin-orbit energy splitting, $\Delta = -\frac{3}{2}\zeta = 0.34$ eV in GaAs, allows us to consider the two j levels independently. In the following we will add a constant offset so that the energies of the pure $j = \frac{3}{2}$ and $j = \frac{1}{2}$ states are equal to 0 and Δ, respectively.

The second term in $\mathcal{H}$ represents the p-d exchange interaction,

$$\mathcal{H}_\text{exch} = \beta \mathbf{M} \cdot (\mathbf{L} + 2\mathbf{S}) = \beta g_j \mathbf{M} \cdot \mathbf{J}, \tag{5}$$

where $\mathbf{M}$ is the mean-field magnetization of the localized Mn $3d$ spins, β is the p-d exchange constant, and

$$g_j = 1 + \frac{j(j+1) + s(s+1) - \ell(\ell+1)}{2j(j+1)} \tag{6}$$

is the Landé g factor. Defining

$$\mathbf{b} \equiv \beta g_j \mathbf{M}, \tag{7}$$

Eq. (5) can be written as

$$\mathcal{H}_\text{exch} = \mathbf{b} \cdot \mathbf{J} = b_z J_z + \frac{1}{2}(b_- J_+ + b_+ J_-). \tag{8}$$

The vector $\mathbf{b}$ is a parameter for exchange interaction with magnitude b and direction $\hat{\mathbf{b}} = \mathbf{b}/b$ and has components b_z and $b_\pm = b_x \pm i b_y$. The Landé g factor makes b dependent on j, but it is constant within each j manifold. The total angular momentum operator $\mathbf{J}$ acts on the magnetic sublevels $|m_j\rangle$ as $J_z|m_j\rangle = m_j|m_j\rangle$ and $J_\pm|m_j\rangle = \sqrt{(J \mp m_j)(J \pm m_j + 1)}|m_j \pm 1\rangle$.

The third term in $\mathcal{H}$ accounts for the strain anisotropy,

$$\mathcal{H}_\text{strain} = c(L_z^2 - \tfrac{1}{3}\mathbf{L}^2) = c(J_z^2 - \tfrac{1}{3}\mathbf{J}^2) = c[m_j^2 - \tfrac{1}{3}j(j+1)], \tag{9}$$

which contains the charge quadrupole operator multiplied by a scalar parameter c for the magnitude of the strain. Finally, the last term in $\mathcal{H}$, for the p-d hybridization, will be considered in Sec. II C 3.

Due to the large spin-orbit interaction, the Hamiltonian $\mathcal{H}$ for the $j = \frac{3}{2}$ level can be blocked out in 4×4 matrix form (four-band model) with basis states $|m_j\rangle = |\frac{3}{2}\rangle$, $|\frac{1}{2}\rangle$, $|-\frac{1}{2}\rangle$, and $|-\frac{3}{2}\rangle$,

$$\mathcal{H}_{3/2} = \begin{pmatrix} \frac{3}{2}b_z + c & \frac{\sqrt{3}}{2}b_- & 0 & 0 \\ \frac{\sqrt{3}}{2}b_+ & \frac{1}{2}b_z - c & b_- & 0 \\ 0 & b_+ & -\frac{1}{2}b_z - c & \frac{\sqrt{3}}{2}b_- \\ 0 & 0 & \frac{\sqrt{3}}{2}b_+ & -\frac{3}{2}b_z + c \end{pmatrix}, \tag{10}$$

with the angular dependence contained in the b components.

For magnetization along the surface normal ($b_z = b$, $b_x = 0$) the Hamiltonian is diagonal with energies E_n^z of

the eigenstates $|m_j\rangle$ as

$$E_1^z = \frac{3}{2}b + c, \tag{11a}$$

$$E_2^z = \frac{1}{2}b - c, \tag{11b}$$

$$E_3^z = -\frac{1}{2}b - c, \tag{11c}$$

$$E_4^z = -\frac{3}{2}b + c. \tag{11d}$$

For in-plane magnetization ($b_x=b$, $b_z=0$) the energies are

$$E_1^x = \frac{1}{2}b + \sqrt{b^2 - bc + c^2}, \tag{12a}$$

$$E_2^x = -\frac{1}{2}b + \sqrt{b^2 + bc + c^2}, \tag{12b}$$

$$E_3^x = \frac{1}{2}b - \sqrt{b^2 - bc + c^2}, \tag{12c}$$

$$E_4^x = -\frac{1}{2}b - \sqrt{b^2 + bc + c^2}. \tag{12d}$$

In order to compare the different states in both directions we first consider the situation that the strain is small compared to the magnetization, in which case we can make a series expansion of the energies E_n^x in Eq. (12) in powers of c,

$$E_1^x = \frac{3}{2}b - \frac{1}{2}c + \frac{3}{8}\frac{c^2}{b} + \mathrm{O}[c]^3, \tag{13a}$$

$$E_2^x = \frac{1}{2}b + \frac{1}{2}c + \frac{3}{8}\frac{c^2}{b} + \mathrm{O}[c]^3, \tag{13b}$$

$$E_3^x = -\frac{1}{2}b + \frac{1}{2}c - \frac{3}{8}\frac{c^2}{b} + \mathrm{O}[c]^3, \tag{13c}$$

$$E_4^x = -\frac{3}{2}b - \frac{1}{2}c - \frac{3}{8}\frac{c^2}{b} + \mathrm{O}[c]^3. \tag{13d}$$

Thus under zero strain ($c \to 0$), where due to the absence of anisotropy the splitting is the same in every direction of $\mathbf{b}$, the states labeled with indices 1, 2, 3, and 4 have eigenvalues equal to $\frac{3}{2}b$, $\frac{1}{2}b$, $-\frac{1}{2}b$, and $-\frac{3}{2}b$, respectively, which is the same in Eqs. (11) and (13). Therefore, these indices uniquely determine the eigenvalues in all directions, and they will be consistently used throughout the paper. Furthermore, Eq. (13) shows that the first-order energy term changes from $\pm c$ in the z-direction to $\mp\frac{1}{2}c$ in the x, y directions, as expected from the zero trace of the quadrupole moment. For thin-film samples the actual strain will be relatively large and the general case is discussed next.

The energies of the valence states for $\mathbf{M}\|z$ and $\mathbf{M}\|x$, given in Eqs. (11) and (12), respectively, are plotted as a function of the magnetization for compressive strain ($c > 0$) in Fig. 3(a) and 3(c) and for tensile strain ($c < 0$) in Fig. 3(b) and 3(d). In order to reduce the energy dependence to a single parameter, we plot E/c as a function of b/c, where b is taken positive. In the four-band model the levels are reversed in energy between compressive

($c > 0$) and tensile strain ($c < 0$), with $E_1(-c) = -E_4(c)$ and $E_2(-c) = -E_3(c)$, as can be verified from Eqs. (11) and (12).

While in Fig. 3(a) and 3(b), E_n^z/c changes linearly with b/c, as given by Eq. (11), the b/c dependence of E_n^x/c in Fig. 3(c) and 3(d) is best understood by making a series expansion of Eq. (12) in b,

$$E_1^x = c + \frac{3}{8}\frac{b^2}{c} + \frac{3}{16}\frac{b^3}{c^2} + \mathrm{O}[b]^4, \tag{14a}$$

$$E_2^x = c + \frac{3}{8}\frac{b^2}{c} - \frac{3}{16}\frac{b^3}{c^2} + \mathrm{O}[b]^4, \tag{14b}$$

$$E_3^x = -c + b - \frac{3}{8}\frac{b^2}{c} - \frac{3}{16}\frac{b^3}{c^2} + \mathrm{O}[b]^4, \tag{14c}$$

$$E_4^x = -c - b - \frac{3}{8}\frac{b^2}{c} + \frac{3}{16}\frac{b^3}{c^2} + \mathrm{O}[b]^4. \tag{14d}$$

This shows for instance that for $b \ll c$ the two levels at $E^x = c$ are degenerate while the two levels at $E^x = -c$ split up with a separation $2b$.

The separation between the state at the valence band maximum and the next state in energy is largest with $\mathbf{M}\|z$ for compressive strain ($c > 0$, where the highest energy is E_1^z), and with $\mathbf{M}\|x$ for tensile strain ($c < 0$, where the highest energy is E_4^x). It is evident that strain causes a pronounced anisotropy of the exchange splitting.

In order to check to correctness of assuming a four-band model, we show in Fig. 3 (dashed lines) also the energies obtained within a six-band model at $k = 0$, using Eqs. (A7)-(A19) of Ref. 13, which takes into account the spin-orbit splitting for GaAs. The 6×6 matrix of the Hamiltonian, used to obtain these energy curves, can be found in Eq. (B1) of App. B. This confirms that, due to the large spin-orbit interaction, there is no significant change in the energies of the four $j = \frac{3}{2}$ levels. The energy reversal of the levels between compressive and tensile strain that occurs in the four-band model is no longer exact in the six-band model. In the latter model the energy values are slightly increased by the interaction with the $j = \frac{1}{2}$ levels.

2. As 4p state magnetic moments

We now proceed to calculate the magnetic moment μ of each state. The XMCD signal is related to the magnetic moment of the unoccupied states.[17,37] The magnetic moment of the As $4p$ state along a given direction can be obtained from the derivative of the energy with respect to the exchange interaction, i.e., $\mu = \partial E(\mathbf{b})/\partial\mathbf{b}$. For the states at the valence-band maximum the derived magnetic moments are shown in Fig. 3(e) for compressive strain ($c > 0$) and in Fig. 3(f) tensile strain ($c < 0$). For small b this corresponds to the level with E_1 for compressive strain and E_4 for tensile strain. For $b/c < -2$ (tensile strain) E_3^z becomes the highest energy [c.f., Fig. 3(b)].

The moment values for μ_1^z, μ_2^z, μ_3^z, and μ_4^z are $\frac{3}{2}$, $\frac{1}{2}$, $-\frac{1}{2}$, and $-\frac{3}{2}$, respectively, as expected from the m_j val-
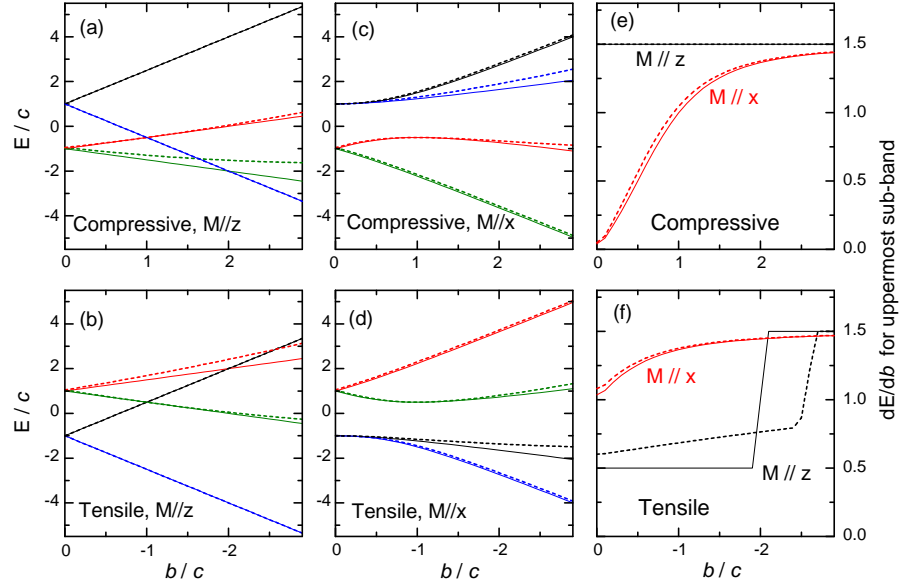
FIG. 3: (Color online) (a-d) Calculated energies of the $j = \frac{3}{2}$ valence state p level as a function of the parameter b/c, for (a) compressive strain, magnetization along z (i.e., perpendicular to the plane); (b) tensile strain, magnetization along z; (c) compressive strain, magnetization along x (i.e., in-plane); (d) tensile strain, magnetization along x. Full lines are obtained using the four-band model with the Hamiltonian in Eq. (10), dashed lines with the six-band model in Eq. (B1). The parameters b and c are the coefficients of the exchange interaction and the strain, respectively. The strain is along the z axis in each case. (e-f) Magnetic moment $\mu = \partial E(\mathbf{b})/\partial \mathbf{b}$ of the uppermost valence subband for the two different magnetization directions, for (e) compressive strain and (f) tensile strain.

ues. For μ^x, the magnetization dependence is most easily visualized by expansion in powers of b,

$$\mu_1^x = \frac{3}{4}\frac{b}{c} + \frac{9}{16}\frac{b^2}{c^2} + \mathrm{O}[b]^3, \tag{15a}$$

$$\mu_2^x = \frac{3}{4}\frac{b}{c} - \frac{9}{16}\frac{b^2}{c^2} + \mathrm{O}[b]^3, \tag{15b}$$

$$\mu_3^x = 1 - \frac{3}{4}\frac{b}{c} - \frac{9}{16}\frac{b^2}{c^2} + \mathrm{O}[b]^3, \tag{15c}$$

$$\mu_4^x = -1 - \frac{3}{4}\frac{b}{c} + \frac{9}{16}\frac{b^2}{c^2} + \mathrm{O}[b]^3. \tag{15d}$$

Figure 3 shows that the anisotropy $\mu^z - \mu^x = \partial E(b_z)/\partial b_z - \partial E(b_x)/\partial b_x$ of the upper level is large when the exchange splitting is comparable to ($b \approx c$) or less than ($b < c$) the strain splitting.

3. Hybridization

Experimentally, the prepeak of the Mn L_3 XMCD is largest when the magnetization is perpendicular-to-plane for tensile strain, and in-plane for compressive strain. Remarkably, this is opposite to the calculated anisotropy of μ at the valence state maximum, as shown in Fig. 3(e) and 3(f). The reason for this is that the XMCD is sensitive to the anisotropy of the p states through the hybridization with the Mn d orbitals.

The Hamiltonian matrix for the p-d hybridization can be written as

$$\mathcal{H}_{\mathrm{hybr}} = \begin{pmatrix} \mathcal{H}_p & V \\ V & \mathcal{H}_d \end{pmatrix}, \tag{16}$$

where $\mathcal{H}_p$ and $\mathcal{H}_d$ are the Hamiltonians for the p and d states and V is the mixing coefficient.

The opposite sign of the anisotropy is because of the charge quadrupole moment $m_\ell^2 - \frac{1}{3}\ell(\ell+1)$ is reversed in the Mn t_2 states compared to the As p states for the magnetization along the same direction. This can be verified by writing down the matrix elements for these states. The Hamiltonian $\mathcal{H} = \mathbf{b}\cdot\mathbf{L} + c(L_z^2 - \frac{1}{3}\mathbf{L}^2)$ for the As p state, with basis $|m_\ell\rangle = |1\rangle$, $|0\rangle$, and $|-1\rangle$, gives

$$\mathcal{H}_p = \begin{pmatrix} b_z + c & \frac{b_-}{\sqrt{2}} & 0 \\ \frac{b_+}{\sqrt{2}} & -2c & \frac{b_-}{\sqrt{2}} \\ 0 & \frac{b_+}{\sqrt{2}} & b_z + c \end{pmatrix}. \tag{17}$$

On the other hand, the same Hamiltonian for the Mn t_2 state, with basis $|m_\ell\rangle = |1\rangle$, $\frac{1}{\sqrt{2}}[|2\rangle - |-2\rangle]$, and $|-1\rangle$, gives

$$\mathcal{H}_{d(t_2)} = \begin{pmatrix} b_z - c & \frac{b_-}{\sqrt{2}} & 0 \\ \frac{b_+}{\sqrt{2}} & 2c & \frac{b_-}{\sqrt{2}} \\ 0 & \frac{b_+}{\sqrt{2}} & b_z - c \end{pmatrix}. \tag{18}$$

Comparison of the matrices in Eqs. (17) and (18) shows that the sign of c is reversed between the As p and Mn t_2

states. The opposite sign of b/c implies a reversal of the magnetic anisotropy, as can be verified from Figs. 3(e) and 3(f). This demonstrates that the strain anisotropy has opposite effect on the magnetic anisotropy between the As p and Mn t_2 valence states, resulting in a reversed sign of the prepeak XMCD anisotropy.

III. CONCLUSIONS

We have given a theoretical analysis of the origin of the Mn L_3 XMCD prepeak in ferromagnetic semiconductors. While the main spectrum arises from the multiplet structure of the Mn d^5 states, which have a cubic anisotropy, the hybridization with the host valence states is revealed by the presence of a distinct prepeak feature with uniaxial anisotropy and marked dependence on the hole density. The XMCD of the prepeak has opposite sign from the main peak since it originates from states near the Fermi level with opposite polarization to the Mn local moment. The L_3 prepeak may be related to the 'impurity band' features reported in angle-resolved photoemission[3] and the pre-edge peak observed in the Mn K edge XMCD.[33] The observation of the L_3 prepeak by element-specific XMCD means that the associate unoccupied state contains Mn $3d$ character and participates in the magnetism. Further evidence that the prepeak corresponds to transitions to the p-d hybridized hole state arises from the increasing prepeak intensity with decreasing hole density, or increasing hole localization. The anisotropy in the XMCD prepeak is positive for compressive strain and negative for tensile strain. This is opposite as for the As p valence state because the hybridized Mn t_2 states have opposite sign of the charge quadrupole moment, and therefore respond oppositely to strain. These experimental observations are confirmed by the described valence-state model, which includes spin-orbit interaction, p-d exchange interaction, strain anisotropy, and p-d hybridization.

These findings provide insight into the interplay of strain and magnetization in ferromagnetic semiconductors. They allow an analysis of both valence state and impurity effects in XMCD. The results clearly demonstrate that the Mn $3d$ states play a role in the anisotropy of the strained ferromagnetic semiconductor.

Appendix A: Angular dependence of XMCD

The local symmetry determines the angular dependence of the XMCD signal. For brevity, we consider only the situation where the x ray helicity vector and magnetization direction are aligned parallel. In cubic symmetry the angular dependence of the XMCD is equal to[21,22]

$$I_{\mathrm{XMCD}}^{\mathrm{cubic}} = I_{\mathrm{iso}} + \left[\frac{1}{4}\left(\sin^4\theta \sin^2 2\phi + \sin^2 2\theta\right) - \frac{1}{5}\right] I_{\mathrm{ani}}, \tag{A1}$$

where θ and ϕ are the polar and azimuthal angle with respect to the [001] axis. I_{iso} and I_{ani} are the isotropic and anisotropic part of the XMCD spectrum, respectively. This results in different XMCD spectra along the various crystallographic directions,

$$I_{\mathrm{XMCD}}^{\langle 001\rangle} = I_{\mathrm{iso}} - \frac{1}{5}I_{\mathrm{ani}}, \tag{A2a}$$

$$I_{\mathrm{XMCD}}^{\langle 011\rangle} = I_{\mathrm{iso}} + \frac{1}{20}I_{\mathrm{ani}}, \tag{A2b}$$

$$I_{\mathrm{XMCD}}^{\langle 111\rangle} = I_{\mathrm{iso}} + \frac{2}{15}I_{\mathrm{ani}}. \tag{A2c}$$

In uniaxial symmetry the angular dependence of the XMCD is equal to[17,37,38]

$$\begin{aligned} I_{\mathrm{XMCD}}^{\mathrm{uniaxial}} &= I_{\mathrm{iso}} + \frac{1}{2}\left(3\cos^2\theta - 1\right) I_{\mathrm{ani}} \\ &= I_z \cos^2\theta + I_x \sin^2\theta, \end{aligned} \tag{A3}$$

where θ is the angle with respect to the uniaxial axis, and

$$I_z = I_{\mathrm{iso}} + I_{\mathrm{ani}}, \tag{A4a}$$

$$I_x = I_{\mathrm{iso}} - \frac{1}{2}I_{\mathrm{ani}}, \tag{A4b}$$

give the XMCD signal along the z (uniaxial axis) and x or y (planar axes) direction, respectively.

The isotropic parts of the cubic and uniaxial XMCD can not be distinguished from each other in the angular dependence. The anisotropic part gives an angular variation of the XMCD that depends on the specific symmetry.

Appendix B: Six-band model

The 6×6 matrix corresponding to the Hamiltonian in the $\mathbf{k} \cdot \mathbf{p}$ model for $k = 0$ with as basis the angular momentum eigenstates $|j = \frac{3}{2}, \frac{1}{2}; m_j = j, \cdots, -j\rangle$ is given by

$$\mathcal{H}_{k=0} = \begin{pmatrix} \frac{3}{2}b_z + c & i\frac{\sqrt{3}}{2}b_x & 0 & 0 & \frac{\sqrt{6}}{2}b_x & 0 \\ -i\frac{\sqrt{3}}{2}b_x & \frac{1}{2}b_z - c & ib_x & 0 & i\sqrt{2}b_z - i\sqrt{2}c & -\frac{\sqrt{2}}{2}b_x \\ 0 & -ib_x & -\frac{1}{2}b_z - c & i\frac{\sqrt{3}}{2}b_x & \frac{\sqrt{2}}{2}b_x & -i\sqrt{2}b_z + i\sqrt{2}c \\ 0 & 0 & -i\frac{\sqrt{3}}{2}b_x & -\frac{3}{2}b_z + c & 0 & -\frac{\sqrt{6}}{2}b_x \\ \frac{\sqrt{6}}{2}b_x & -i\sqrt{2}b_z + i\sqrt{2}c & \frac{\sqrt{2}}{2}b_x & 0 & -\frac{1}{2}b_z + \Delta & \frac{i}{2}b_x \\ 0 & -\frac{\sqrt{2}}{2}b_x & i\sqrt{2}b_z - i\sqrt{2}c & -\frac{\sqrt{6}}{2}b_x & -\frac{i}{2}b_x & \frac{1}{2}b_z + \Delta \end{pmatrix} . \tag{B1}$$

This gives the eigenenergies shown by the dashed lines in Fig. 3. The matrix reduces to a 4×4 matrix for $j = \frac{3}{2}$ in Eq. (10) [which corresponds to the upper-left block of the matrix in Eq. (B1)] when the spin-orbit splitting Δ (= 0.34 eV in GaAs) is much larger than the coefficients b and c of the exchange interaction and the strain, respectively. For the four-band model the eigenenergies are given by the solid lines in Fig. 3.

[1] B. Beschoten, P. A. Crowell, I. Malajovich, D. D. Awschalom, F. Matsukura, A. Shen, and H. Ohno, Phys. Rev. Lett. **83**, 3073 (1999).

[2] S. Sanvito, P. Ordejon, and N. A. Hill, Phys. Rev. B **63**, 165206 (2001).

[3] J. Okabayashi, A. Kimura, O. Rader, T. Mizokawa, A. Fujimori, T. Hayashi, and M. Tanaka, Phys. Rev. B **64**, 125304 (2001).

[4] D. J. Keavney, D. Wu, J. W. Freeland, E. Johnston-Halperin, D. D. Awschalom, and J. Shi, Phys. Rev. Lett. **91**, 187203 (2003).

[5] P. Mahadevan and A. Zunger, Phys. Rev. B **69**, 115211 (2004).

[6] K. S. Burch, D. B. Shrekenhamer, E. J. Singley, J. Stephens, B. L. Sheu, R. K. Kawakami, P. Schiffer, N. Samarth, D. D. Awschalom, and D. N. Basov, Phys. Rev. Lett. **97**, 087208 (2006).

[7] K. Ando, H. Saito, K. C. Agarwal, M. C. Debnath, and V. Zayets, Phys. Rev. Lett. **100**, 067204 (2008).

[8] M. Sawicki, D. Chiba, A. Korbecka, Y. Nishitani, J. A. Majewski, F. Matsukura, T. Dietl, and H. Ohno, Nature Physics **6**, 22 (2010).

[9] V. N. Antonov, A. N. Yaresko, and O. Jepsen, Phys. Rev. B **81**, 075209 (2010).

[10] M. Sawicki, F. Matsukura, A. Idziaszek, T. Dietl, G. M. Schott, C. Ruester, C. Gould, G. Karczewski, G. Schmidt, and L. W. Molenkamp, Phys. Rev. B **70**, 245325 (2004).

[11] M. Abolfath, T. Jungwirth, J. Brum, and A. H. MacDonald, Phys. Rev. B **63**, 054418 (2001).

[12] T. Jungwirth, J. Masek, K. Y. Wang, K. W. Edmonds, M. Sawicki, M. Polini, J. Sinova, A. H. MacDonald, R. P. Campion, L. X. Zhao, et al., Phys. Rev. B **73**, 165205 (2006).

[13] T. Dietl, H. Ohno, and F. Matsukura, Phys. Rev. B **63**, 195205 (2001).

[14] T. Jungwirth, K. Y. Wang, J. Masek, K. W. Edmonds, J. König, J. Sinova, M. Polini, N. A. Goncharuk, A. H. MacDonald, M. Sawicki, et al., Phys. Rev. B **72**, 165204 (2005).

[15] B. T. Thole, P. Carra, F. Sette, and G. van der Laan, Phys. Rev. Lett. **68**, 1943 (1992).

[16] P. Carra, B. T. Thole, M. Altarelli, and X. Wang, Phys. Rev. Lett. **70**, 694 (1993).

[17] G. van der Laan, Phys. Rev. B **57**, 112 (1998).

[18] H. A. Dürr, G. Y. Guo, G. van der Laan, J. Lee, G. Lauhoff, and J. A. C. Bland, Science **277**, 213 (1997).

[19] A. A. Freeman, K. W. Edmonds, G. van der Laan, N. R. S. Farley, T. K. Johal, E. Arenholz, R. P. Campion, C. T. Foxon, and B. L. Gallagher, Phys. Rev. B **73**, 233303 (2006).

[20] A. A. Freeman, K. W. Edmonds, G. van der Laan, R. P. Campion, A. W. Rushforth, N. R. S. Farley, T. K. Johal, C. T. Foxon, B. L. Gallagher, A. Rogalev, et al., Phys. Rev. B **77**, 073304 (2008).

[21] K. W. Edmonds, G. van der Laan, A. A. Freeman, N. R. S. Farley, T. K. Johal, R. P. Campion, C. T. Foxon, B. L. Gallagher, and E. Arenholz, Phys. Rev. Lett. **96**, 117207 (2006).

[22] K. W. Edmonds, G. van der Laan, N. R. S. Farley, E. Arenholz, R. P. Campion, C. T. Foxon, and B. L. Gallagher, Phys. Rev. B **77**, 113205 (2008).

[23] F. Maccherozzi, M. Sperl, G. Panaccione, J. Minar, S. Polesya, H. Ebert, U. Wurstbauer, M. Hochstrasser, G. Rossi, G. Woltersdorf, et al., Phys. Rev. Lett. **101**, 267201 (2008).

[24] K. Olejnik, P. Wadley, J. A. Haigh, K. W. Edmonds, R. P. Campion, A. W. Rushforth, B. L. Gallagher, C. T. Foxon, T. Jungwirth, J. Wunderlich, et al., Phys. Rev. B **81**, 104402 (2010).

[25] K. W. Edmonds, N. R. S. Farley, T. K. Johal, G. van der Laan, R. P. Campion, B. L. Gallagher, and C. T. Foxon, Phys. Rev. B **71**, 064418 (2005).

[26] G. van der Laan and B. T. Thole, Phys. Rev. B **43**, 13401 (1991).

[27] P. R. Stone, M. A. Scarpulla, R. Farshchi, I. D. Sharp, E. E. Haller, O. D. Dubon, K. M. Yu, J. W. Beeman, E. Arenholz, J. D. Denlinger, et al., Appl. Phys. Lett. **89**, 012504 (2006).

[28] R. D. Cowan, *The Theory of Atomic Structure and Spectra* (University of California Press, Berkeley, 1982).

[29] A correction factor of 1.47 is applied to the obtained spin moment, to account for mixing of the $2p_{3/2}$ and $2p_{1/2}$ multiplets. This is obtained by applying the spin sum rule (Ref. 16) to calculated Mn d^5 multiplet spectra with known values of the spin moment. For further details, see Ref. 25.

[30] H. Ohldag, V. Solinus, F. U. Hillebrecht, J. B. Goedkoop, M. Finazzi, F. Matsukura, and H. Ohno, Appl. Phys. Lett. **76**, 2928 (2000).

[31] F. Kronast, R. Ovsyannikov, A. Vollmer, H. A. Dürr, W. Eberhardt, P. Imperia, D. Schmitz, G. M. Schott, C. Ruester, C. Gould, et al., Phys. Rev. B **74**, 235213 (2006).

[32] G. van der Laan, Lect. Notes Phys. **697**, 199 (2006).

[33] P. Wadley, A. A. Freeman, K. W. Edmonds, G. van der Laan, J. S. Chauhan, R. P. Campion, A. W. Rushforth, B. L. Gallagher, C. T. Foxon, F. Wilhelm, et al., Phys. Rev. B **81**, in print (2010).

[34] W. W. Chow, S. W. Koch, and M. Sargent, *Semiconductor-Laser Physics* (Springer-Verlag, Heidelberg, 1994).

[35] M. Sawicki, J. Magn. Magn. Mater. **300**, 1 (2006).

[36] S. S. Dhesi, G. van der Laan, E. Dudzik, and A. B. Shick, Phys. Rev. Lett. **87**, 067201 (2001).

[37] G. van der Laan, B. T. Thole, G. A. Sawatzky, J. B. Goedkoop, J. C. Fuggle, J. M. Esteva, R. C. Karnatak, J. P. Remeika, and H. A. Dabkowska, Phys. Rev. B **34**, 6529 (1986).

[38] G. van der Laan, J. Phys.: Condens. Matter **13**, 11149 (2001).